

Quantitative Analysis of Hydrogen-Assisted Microcracking in Duplex Stainless Steel through X-Ray Refraction 3D Imaging

René Laquai, Thomas Schaupp, Axel Griesche, Bernd R. Müller,* Andreas Kupsch, Andreas Hannemann, Thomas Kannengiesser, and Giovanni Bruno

While the problem of the identification of mechanisms of hydrogen-assisted damage has and is being thoroughly studied, the quantitative analysis of such damage still lacks suitable tools. In fact, while, for instance, electron microscopy yields excellent characterization, the quantitative analysis of damage requires at the same time large field-of-views and high spatial resolution. Synchrotron X-ray refraction techniques do possess both features. Herein, it is shown how synchrotron X-ray refraction computed tomography (SXRCT) can quantify damage induced by hydrogen embrittlement in a lean duplex steel, yielding results that overperform even those achievable by synchrotron X-ray absorption computed tomography. As already reported in the literature, but this time using a nondestructive technique, it is shown that the hydrogen charge does not penetrate to the center of tensile specimens. By the comparison between virgin and hydrogen-charged specimens, it is deduced that cracks in the specimen bulk are due to the rolling process rather than hydrogen-assisted. It is shown that (micro)cracks propagate from the surface of tensile specimens to the interior with increasing applied strain, and it is deduced that a significant crack propagation can only be observed short before rupture.

economic and design aspects are leading to ever higher requirements in terms of resistance to corrosive media and materials strength. Where corrosion-resistant austenitic stainless steels were used in the past, austenitic–ferritic duplex stainless steels (DSS) are now increasingly being applied.^[1] DSS are used, for example, in the chemical and petrochemical industries, in shipbuilding and plant construction, as well as in offshore industry. The construction industry increasingly uses DSS. In the context of lightweight construction, the use of DSS allows enormous weight savings compared to austenitic stainless steels. These steels combine the very good chemical resistance of the austenitic stainless steels with the higher strength of the ferritic stainless steels.^[1,2] The adjustment of the austenite to δ -ferrite ratio to 50:50 is controlled by the alloying elements, especially nitrogen, and thermomechanical treatments.

1. Introduction

The demands placed on steels, particularly in the field of aggressive environments, have risen steadily in recent decades. Both

Despite the outstanding mechanical and corrosive properties, cases of damage associated with the negative effects of hydrogen are reported to have occurred in many industrial sectors. These take place in the form of degradation of the mechanical properties by hydrogen embrittlement (HE). Furthermore, this damage can lead to hydrogen-assisted cracking (HAC) at a given critical combination of microstructure, strain, and hydrogen concentration. The absorption of hydrogen into the material structure occurs, for example, via cathodic protection of pipelines in seawater^[3] or when the material is used in extremely acid environments with very low pH.^[4]

The degradation of mechanical properties in steels in the presence of hydrogen is explained in several pioneering publications, and the reader is referred to ref. [5] and the references contained therein.


HAC is well described for ferritic^[6] and austenitic^[7] materials. Moreover, recently Claeys et al.^[8] have also thoroughly studied HAC in DSS, in spite of the difficulty that two phases are present at the same time, differently interacting with hydrogen.

The mechanisms of HAC in austenitic–ferritic DSS are sometimes debated. Some authors state that damage is very likely to occur first in the ferritic phase of the DSS, but actually Claeys et al.^[8] find the opposite. In the work of Nilsson and Chai,^[9] it was shown that the cracks in the ferritic phase initiate

R. Laquai, T. Schaupp, A. Griesche, B. R. Müller, A. Kupsch, A. Hannemann, T. Kannengiesser, G. Bruno
Bundesanstalt für Materialforschung und -prüfung (BAM)
Unter den Eichen 87, 12205 Berlin, Germany
E-mail: bernd.mueller@bam.de

R. Laquai
Physikalisch-Technische Bundesanstalt
Bundesallee 100, 38116 Braunschweig, Germany

G. Bruno
Institute of Physics and Astronomy
University of Potsdam
Karl-Liebknecht-Str. 24-25, 14476 Potsdam, Germany

 The ORCID identification number(s) for the author(s) of this article can be found under <https://doi.org/10.1002/adem.202101287>.

© 2022 The Authors. Advanced Engineering Materials published by Wiley-VCH GmbH. This is an open access article under the terms of the Creative Commons Attribution License, which permits use, distribution and reproduction in any medium, provided the original work is properly cited.

DOI: 10.1002/adem.202101287

Table 1. Chemical composition in wt% and mechanical properties of the material X2CrMnNiN21-5-1.

Chemical composition in wt% (measured by spark emission spectroscopy)						
C	Mn	Cr	Mo	Ni	[N]	Fe
0.02	4.88	20.96	0.18	1.54	0.17	Rest
Mechanical properties according to EN 10 088-2						
Yield strength			Ultimate tensile strength		Elongation	
$R_{p0.2}$ in MPa			R_m in MPa		A in %	
min. 530			700–900		min. 30	

preferentially at grain boundaries or at the phase boundary with austenite, but Claeys et al.^[8] show that both inter- and intragranular damage can occur. In fact, while the deformation and damage mechanisms have attracted quite some attention (see the works of Marinelli et al.,^[10] San Marchi et al.,^[11] Oltra et al.,^[12] Sobol et al.,^[13] and Golebiowski et al.^[14]), this subject is not treated in the present work. Rather, we focus on the quantitative characterization of damage, which has represented a great challenge until now. In fact, the detection of individual cracks needs high-resolution (imaging) methods (the grain size of the phases in DSS is of the order of 10 μm), while a sound statistical analysis requires a large number of defects to be detected (imaged), and therefore, a large field-of-view (FoV).

There are several methods to characterize HAC. Liang et al.^[15] used neutron diffraction to describe the dissimilar susceptibility of austenite and ferrite of a DSS in hydrogen-charged condition. Castellote et al.^[16] also used nuclear resonance analysis on a ferrite–cementite high strength steel to measure the hydrogen concentration profile as a function of depth from the fracture surface and neutron diffraction to investigate the phase content. Their conclusions remained at the global specimen scale. Many other studies used electron back-scattering diffraction (EBSD) to locate cracks and arbitrate on their origin.^[8] Holroyd et al.^[17] have extensively used fractography to investigate the origin of rupture and the mechanisms of embrittlement of an Al alloy (5xxx series). They also used X-ray computed tomography (XCT) to complement their results. In fact, microscopy-based techniques often require very time-consuming specimen preparation and experiments and are always limited to surface investigations. Instead, XCT allows investigating the bulk of specimens in a nondestructive fashion. XCT has been used by Eguchi et al., who managed to image damage in a 2202 lean duplex steel specimen.^[18] In order to obtain high-resolution images, they had to use very small wires (about 300 μm diameter). As they used laboratory XCT (pixel size of 1.64 μm), they had to heavily rely on scanning electron microscope (SEM) pictures to disclose the origin of fracture. In fact, if one wants high-resolution XCT, only synchrotron radiation computed tomography (SXCT) can offer a quantitative solution. However, the higher the resolution, the smaller is the specimen size and the lower is the statistical relevance of the investigation. Alternatives offering a large FoV and a high resolution are welcome.

Synchrotron X-ray refraction computed tomography (SXRCT) provides a suitable solution to the challenge posed above: it is a nondestructive technique, it allows investigating large FoVs, and it enables the detection of cracks with sizes below the spatial resolution of most advanced imaging systems. In fact, the

minimum object size detectable has been estimated at about 1 nm^[19]; understandably, the technique requires a large number of small defects (objects) to yield signal above the background level, and cannot image a single defect at the nanoscale. In other words, the spatial resolution of SXRCT remains limited by that of the detector, but SXRCT can detect a much larger amount of defects. This has been proven in several publications,^[20] and we have already successfully used this method to detect cracks in duplex structures.^[21]

The objective of this work is to detect and quantitatively evaluate HAC in a 2101 lean DSS. 3D tomographic reconstructions are used to determine the size and location of the cracks in hydrogen-charged tensile specimens subjected to different load levels (plastically deformed and fully fractured). We will see that SXRCT can offer complementary and even a greater wealth of information to SXCT.

2. Experimental Section

A 6 mm thick cold-rolled plate of a 2101 lean DSS X2CrMnNiN21-5-1 (1.4162) was investigated. The chemical composition and the nominal mechanical properties of the material are listed in Table 1. Figure 1 shows the microstructural

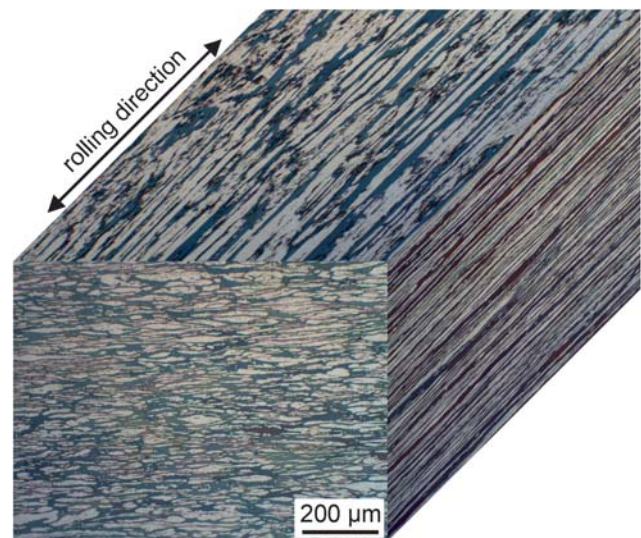


Figure 1. Microstructural orientation of the δ -ferrite (dark) and γ -austenite (bright).

distribution of the different phases in the plate. Expectedly, grains of both austenite and ferrite phase are elongated along the rolling direction. Importantly, no hint to austenite–martensite phase transformation was found in micrographs of the hydrogen-charged and loaded specimens (pictures not shown). In addition to the microstructural orientation, the volume fraction of the phases was also determined by etching (Beraha II reagent) a dedicated specimen and determining the volume fractions with image analysis (software IMS, Imagic, Glattbrugg, Switzerland) of five areas in different orientations. The present lean DSS has a phase ratio of 54% δ -ferrite to 46% austenite and is very close to the optimum phase ratio of 50:50.

Round tensile specimens were machined out in the rolling direction by turning. This caused the formation of cracks perpendicular to the loading direction in tensile tests with hydrogen-charged specimens as already shown in previous studies.^[4,11,22] The geometry of the tensile specimens is illustrated in **Figure 2**. The gauge area was set to be 1.5 mm in diameter to ensure enough transmission for the computed tomography (see below) and was manufactured to final dimensions by means of cylindrical grinding.

For hydrogen charging, a galvanostatic charging cell (current density: 8 mA cm^{-2}) was used. Specimens (acting as cathodes) were placed in an aqueous solution containing 0.1 M H_2SO_4 and 0.05 M NaAsO_2 and charged for 120 h (sodium arsenate was added as an inhibitor to prevent hydrogen recombination at the specimen surface). Immediately after hydrogen charging, the specimens were stored in liquid nitrogen at -196°C to prevent hydrogen desorption and effusion.

The specimens (including an uncharged one) were then subjected to tensile tests after defrosting in acetone to room temperature for 1 min. A constant displacement rate of 1.67 mm min^{-1} was used. The two split parts of all ruptured specimens were kept for further analysis:

For the charged specimens, one part was used for X-ray refraction tomography investigations (see below) and the other for the determination of the hydrogen amount. The latter was carried out by means of carrier gas hot extraction (CGHE) technique using a G8 GALILEO analyzer from Bruker AXS GmbH.^[23] All specimens also underwent X-ray absorption tomography (SXCT) investigations (see below).

For the 3D analysis of the local distribution and amount of microcracking SXRCT was carried out at BAMline, the hard X-ray imaging beamline installed at the synchrotron BESSY II (Helmholtz-Zentrum Berlin).^[24]

SXRCT is an advanced 3D X-ray imaging technique, which exploits the refraction of X-rays at interfaces between materials with different refraction indices to detect cracks smaller than the spatial resolution of the imaging system.^[20b] X-ray refraction radiography and tomography were developed for lightweight, microstructured materials, in which the (poor) absorption contrast was not sufficient to obtain good density resolution. Indeed, X-ray refraction is the physical phenomenon behind all phase-contrast methods used in classic X-ray tomography (SXCT). Moreover (or consequently), X-ray refraction techniques are sensitive to nanometric objects (if present in sufficient quantity) and can image fields of view much larger than SXCT. The principle is the same as that of synchrotron X-ray refraction radiography (SXRR)^[25] and uses an analyzer crystal (Si(111) single crystal) placed between the specimen and the detector to filter the X-rays according to their propagation direction by means of Bragg diffraction. The basic setup is presented in **Figure 3**.

By scanning the rocking curve of the analyzer crystal (over a small angular tilt range, typically about $1'$ of arc), the divergence of the X-rays is analyzed. Refraction events within the specimen cause X-rays to be deflected from their original path and, thus, the X-ray divergence is increased with respect to the free X-ray beam, called the flat field image. However, the analyzer crystal only discriminates the X-rays within its scattering plane (y - z -plane in **Figure 3**) and, therefore, only cracks oriented within the x - z -plane in **Figure 3**, with a tolerance of about $\pm 45^\circ$, can be detected. For practical reasons, it is not possible to sample a complete rocking curve for each projection angle of a tomographic scan. Therefore, the analyzer crystal is adjusted to the maximum of its rocking curve for the SXRCT measurement. At this setting, all X-rays, which are deflected by refraction events within the specimen, are rejected by the analyzer crystal causing an additional attenuation of the X-rays in the projections on top of the attenuation described by the linear attenuation coefficient μ . This effect is described by adding the refraction value C_m to the exponent of Lambert–Beer's law of attenuation. The X-ray intensity I_{\max} measured at the maximum of the rocking curve is, therefore, described by the following equation, where $I_{\max,0}$ is the incident X-ray intensity at the maximum of the rocking curve and d is the thickness of the specimen.

$$I_{\max} = I_{\max,0} \cdot e^{-(\mu+C_m) \cdot d} \quad (1)$$

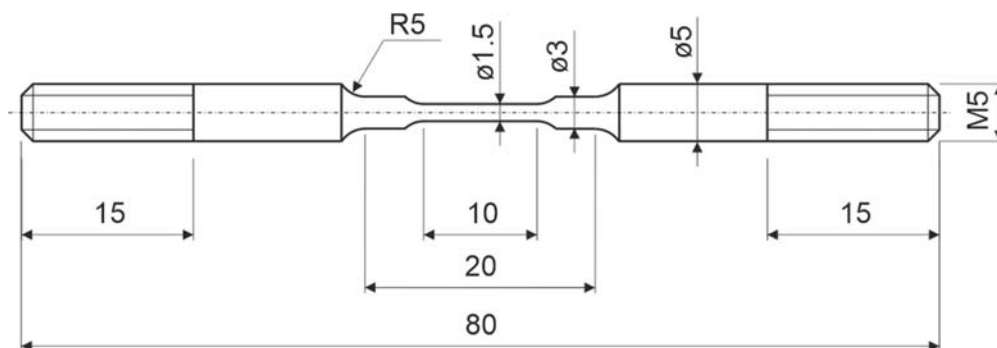


Figure 2. Geometry of round tensile specimen; machined with tensile axis parallel to the rolling direction of the steel plate (all dimensions in mm).

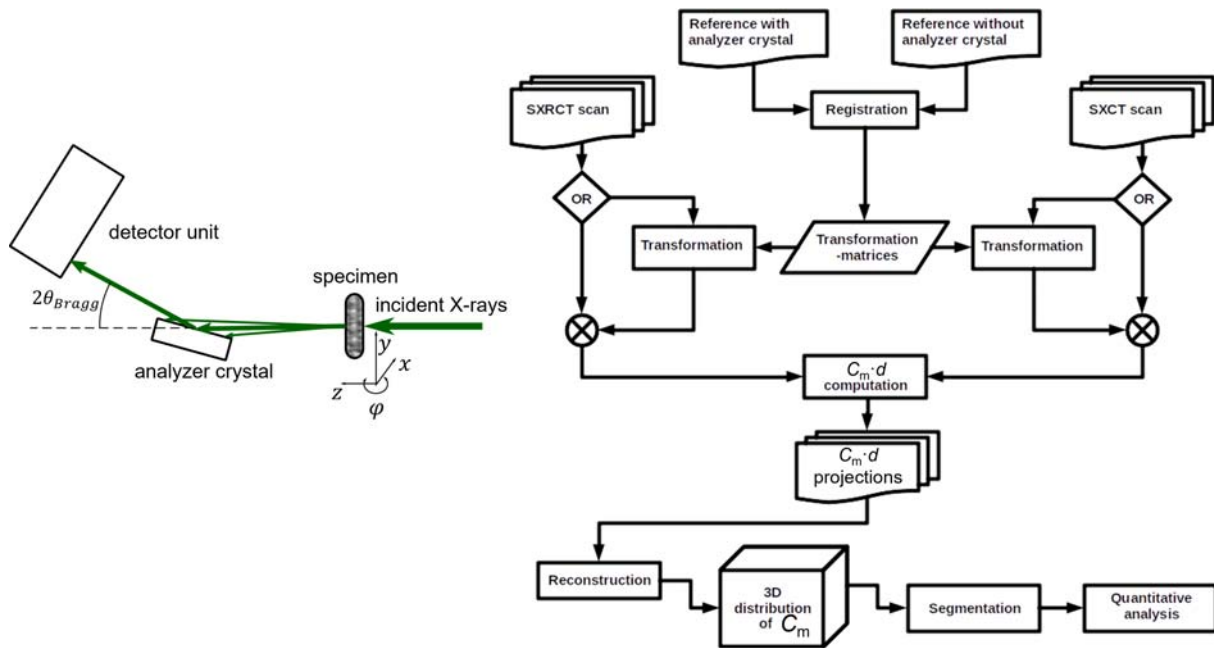


Figure 3. Schematic representation of the experimental setup (left: all the rays reflected by the crystal are shown by the thick arrow, while the rays deflected in all directions in the sample and not reflected by the crystal are shown by the two thin arrows) and image processing chain (right) of SXRCT.

To determine the refraction value C_m , a second synchrotron X-ray computed tomography (SXCT) scan without the analyzer crystal is performed. The projections in such scan yield the total transmitted X-ray intensity I_{trans} , which is determined by the linear attenuation coefficient μ and the incident beam intensity $I_{\text{trans},0}$.

$$I_{\text{trans}} = I_{\text{trans},0} \cdot e^{-\mu \cdot d} \quad (2)$$

Using the series expansion of the logarithm, the refraction value C_m is then expressed as follows.^[26]

$$C_m = \frac{1}{d} \left(1 - \frac{I_{\text{max}} \cdot I_{\text{trans},0}}{I_{\text{max},0} \cdot I_{\text{trans}}} \right) \quad (3)$$

To reconstruct the 3D distribution of the refraction value C_m , projections representing the quantity $C_m \cdot d$ are required. For this purpose, both CT scans—with and without analyzer crystal—are registered to each other and then processed together accordingly. For the registration, the transformation between the two imaging setups—with and without analyzer crystal—is determined on a reference object, i.e., a brass grid, and then applied to the entire stack of projections of both CT scans. The precision of the registration using this procedure is smaller

than $\frac{1}{3}$ of the pixel size. Such precision is sufficient for the present purposes. The reconstruction was performed using the custom filtered backprojection software of BAM. The entire image processing workflow is visualized in Figure 3. Further information about the imaging technique can be found in previous studies.^[26,27]

For the measurements performed in this study, the photon energy was set to 50 keV using a Si(111) double-crystal monochromator. This yielded a minimum transmission of about 10% (this value is close to the lower limit to acquire images with sufficient information). The X-ray detector consisted of a CdWO_4 scintillator, a macroscope, and a 2048×2048 pixel CCD camera with an effective pixel size of $3.6 \mu\text{m}$. The primary beam was narrowed to the detector FoV ($7 \times 7 \text{mm}^2$) to suppress detector backlighting.^[28] Both the SXRCT and the SXCT scans were performed with 1440 projections evenly distributed over a 360° rotation of the specimens.

For further characterization of HE and cracking, the fracture surfaces of hydrogen free and hydrogen-charged specimens were studied with the SEM VEGA3 from TESCAN ANALYTICS with an acceleration voltage of 20 kV and working distances of 8.25 mm for specimen A, 10.29 mm for B, and 10.57 mm for C. Table 2 gives an overview of the investigations performed.

Table 2. Overview of tensile specimens and corresponding investigations.

Specimen	Hydrogen charging time in h	Deformation	CGHE + MS	SEM	SXCT	SXRCT
A	–	Fracture	–	x	x	x
B	120	Plastic	x	–	x	x
C	120	Fracture	x	x	x	x

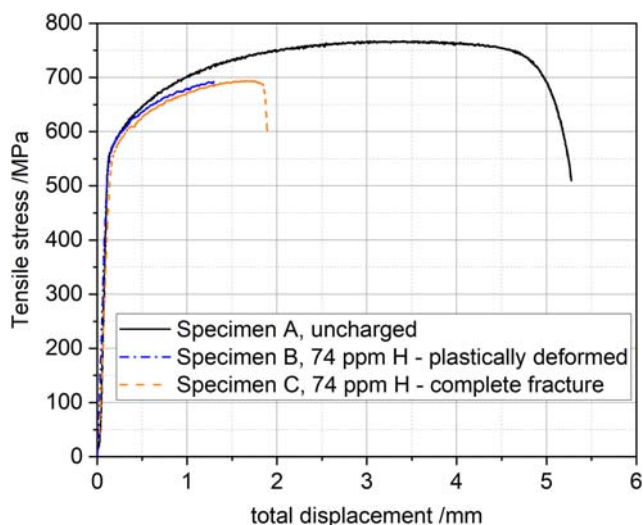


Figure 4. Tensile stress versus total displacement for specimens in uncharged and hydrogen-charged condition.

3. Results and Discussion

3.1. Fracture Topography

After 120 h of hydrogen charging, a total hydrogen concentration of 78 ppm was measured. Of this, 74 ppm is present as reversible (diffusible) hydrogen and 4 ppm as irreversible, trapped, hydrogen. Studies previously conducted on the same material showed a total hydrogen concentration of 198 ppm after a charging time of 168 h.^[21] These data confirm that longer charging times result in higher hydrogen concentrations. **Figure 4** shows the results of the tensile tests of all specimens. The effect of degradation can be clearly seen: In hydrogen-free condition (specimen A), the ultimate tensile strength is 767 MPa, while with a hydrogen concentration of 74 ppm the strength is reduced to 692 MPa (specimen C). Furthermore, a significant decrease in total displacement occurs, indicating a significant decrease in ductility. For the sake of reproducibility, a further specimen (B) was deformed into the plastic region, but without reaching rupture. Its stress–elongation curve follows that of specimen C.

Figure 5 shows the topography of fracture surfaces characterized by SEM. The entire fracture topography of specimen A in

hydrogen-free condition was ductile with microvoid coalescence (MVC) and ductile dimples (see **Figure 5a**). Only in the center of the section some cracks were observed. We can assume that such cracks are due to segregations (impurities). Interestingly, the deformed specimen A cross section was oval, indicating a strong anisotropy of the cold-rolled duplex microstructure (see **Figure 1**). The fracture topography of the hydrogen-charged specimen C is shown in **Figure 5b,c**. The edge and the center show different features: In the center, a mixed topography with brittle fracture and ductile dimples (MVC) is visible, together with macrocracks. Analogous to specimen A, cracking is due to segregation. In the edge region of the specimen, a fully brittle fracture topography is observed (see **Figure 5c**). As also reported in Claeys et al.,^[8b] complete hydrogen saturation did not occur in specimen C (hydrogen concentration 74 ppm). In a previous work, we showed that if the hydrogen concentration is increased to 193 ppm, there is complete hydrogen saturation over the entire specimen cross section and a brittle fracture surface occurs over the whole cross section.^[21]

3.2. Synchrotron Refraction and Transmission Tomography

The SXRCT and SXCT measurements reveal that in all investigated specimens cracks appear predominantly at the outer edges of the specimen and the amount as well as the size of these cracks increase with increasing mechanical load (specimens C versus B) and increasing hydrogen content (specimens B and C vs A). **Figure 6** shows projections of reconstructed slices of specimens B and C along the center axis, i.e., the loading direction, of the reconstructed 3D distribution of the refraction value C_m and the linear attenuation coefficient μ . The comparison of the different specimens shows that the cracks at the outer surface of the specimen grow with increasing load, while the defects closer to the center are largely unaffected by the load increase. Both imaging modes, SXRCT and SXCT, seem to show the same amount of defects at a first glance. However, the number of defects found by the two methods differs significantly. In the SXRCT reconstructed volumes, 159 defects can be found for specimen B and 602 for specimen C, while in SXCT reconstructed volumes only 74 and 373 defects are found, respectively. Note that for specimen A only eight defects could be observed, so we can safely consider specimen A as defect-free. In fact, the

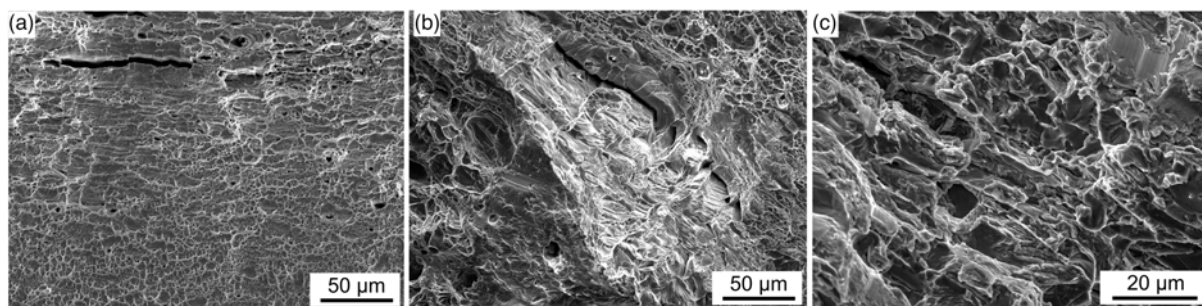


Figure 5. a) Fracture topography of a center region in specimen A (uncharged conditions). b) Fracture topography of specimen C in the center, and c) at the edge.

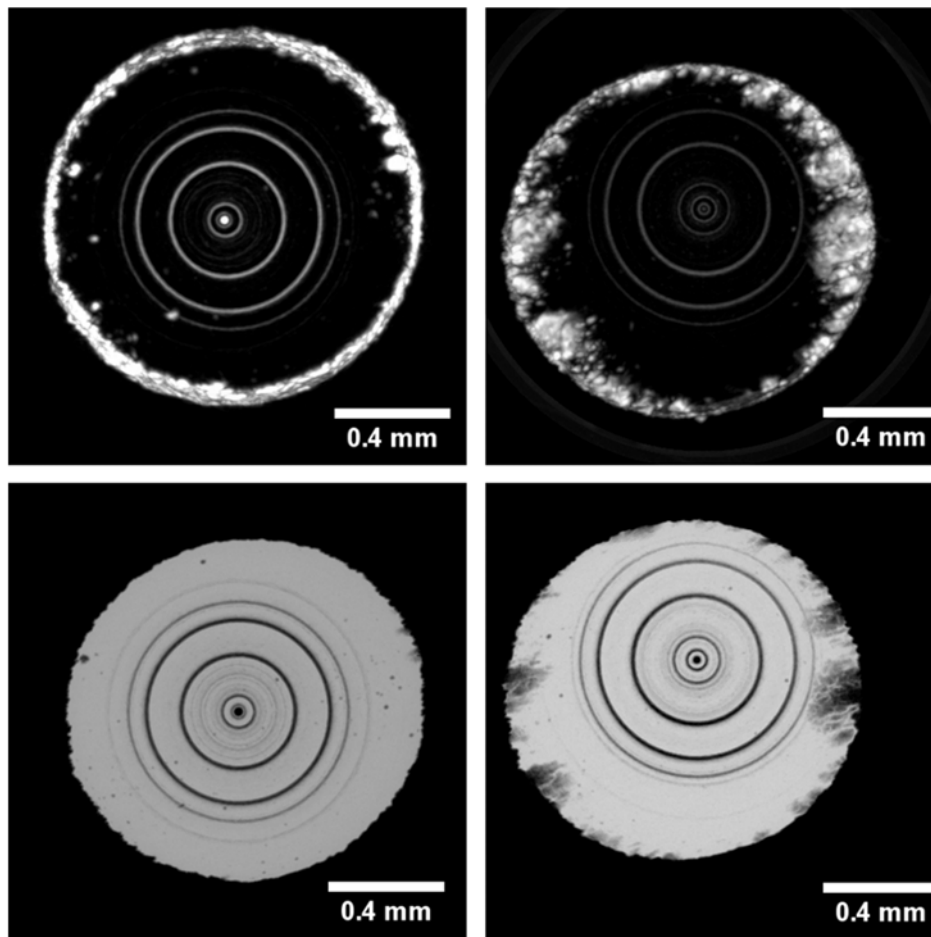


Figure 6. Integration of all reconstructed slices along the cylinder axis (the slices perpendicular to the specimen axis are summed up) of specimens B (left) and C (right) obtained by SXRCT (top) and SXCT (bottom). The circular features are ring artifacts caused by defects in the scintillator screen. Such artifacts could not be removed without also removing some of the defects.

detectability of defects is limited to the spatial resolution in SXCT: the smallest detectable object corresponds to the smallest object that can be imaged. This is not the case for SXRCT, where detectability is enhanced by the refraction phenomenon (also known as phase contrast in the XCT community, see, e.g., Soares et al.^[29]). In our case, the better contrast of the SXRCT images with respect to the SXCT ones allowed us also to image more individual defects (at the same spatial resolution).

Unlike SEM pictures (because of the small FoV), SXRCT allows a robust statistical analysis of the defects. For quantitative analysis, the defects were segmented in the SXRCT data (see **Figure 7**), and their size and location within the specimen were extracted. Segmentation was performed using the advanced surface determination of the image processing software VG Studio MAX (Volume Graphics, Heidelberg, Germany). As a measure of the crack size, the diameter of the smallest sphere circumscribing the entire defect (pore or crack) was determined. This corresponds to the largest extension of the defect in any direction and is equivalent to the length of the crack in case of very elongated defects. The locations of the cracks were determined as their smallest distance from the outer surface of the specimen. In

Figure 8, histograms of the crack size and location are plotted for specimens B and C.

The histograms show that the average size of the cracks (37 μm in diameter) does not significantly change between the two mechanical loading stages (specimens B and C). In both specimens, the mode of the crack size is about 25 μm (**Figure 8**, top row). However, the number of cracks increases significantly with increased applied load. Interestingly, in specimen C several cracks are observed with crack sizes larger than 100 μm and even up to 300 μm . Such cracks are not observed in specimen B. This effect is due to simple crack propagation near failure.

The defect distance to the outer surface (depth in **Figure 8**) is slightly larger in specimen C: In specimen B, most cracks occur within 20 μm from the outer surface with very few occurring at depths larger 40 μm . In specimen C, a significant number of cracks occur at depths of up to 120 μm . Because of the gradient of the hydrogen content, cracks first appear at a smaller distance to the outer surface of the specimen where the hydrogen content is higher (specimen B). As the load increases, damage progresses further into the specimen and the amount of cracking as well as

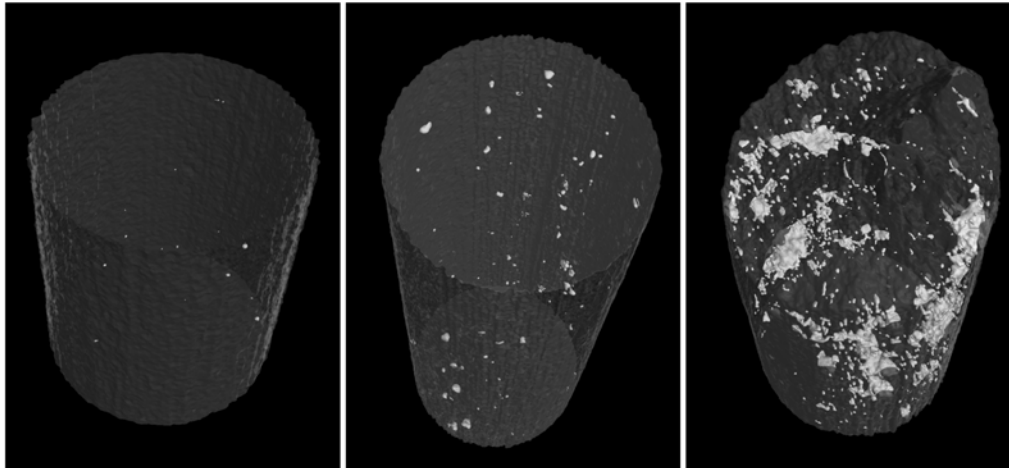


Figure 7. 3D rendering of cracks in specimens A (left), B (center), and C (right) obtained from the reconstructed volume of refraction values C_m .

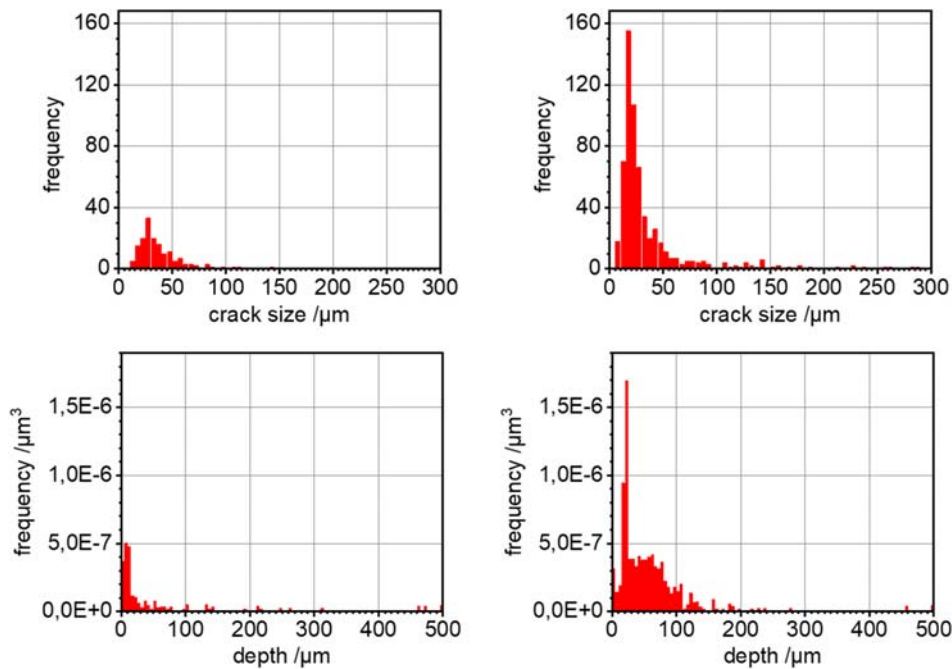


Figure 8. Histograms showing the distribution of crack sizes (top) as a function of depth, i.e., distance from the outer surface of the specimen (bottom), in specimens B (left) and C (right) obtained from SXRCT measurements. The top row shows the frequencies; the bottom row shows the volume-normalized frequencies.

the penetration depth of damage in specimen C become larger than in specimen B. By normalizing the distributions in the top row of Figure 8 to the corresponding volume (i.e., by dividing the frequencies by $2\pi r \cdot \Delta r$, with r = distance from the center, Δr = width of the annular ring on which data are integrated, and the sample height), we can observe that the largest cracks (volumes) occur in the subsurface regions.

In the center of both specimen B and specimen C, there are almost no cracks detected by SXRCT. This is visualized in **Figure 9**, where the occurrence of cracks is depicted on different

unrolled shells of the deformed cylinders (note that the pictures at 120 μm depth must be considered as the deepest possible; in fact, unrolling a shell near the center of the specimen would not yield much information because the actual surface of the shell would be small). It is to note that the cross section of the gauge volume is deformed to an elliptical one. In case of specimen B the ratio of axes is 1:1.02 (short axis 1.29 mm), in case of specimen C 1:1.06 (short axis 1.23 mm and consistent with the results of fracture topography, Section 3.1). Moreover, the segmented surfaces are very rough.

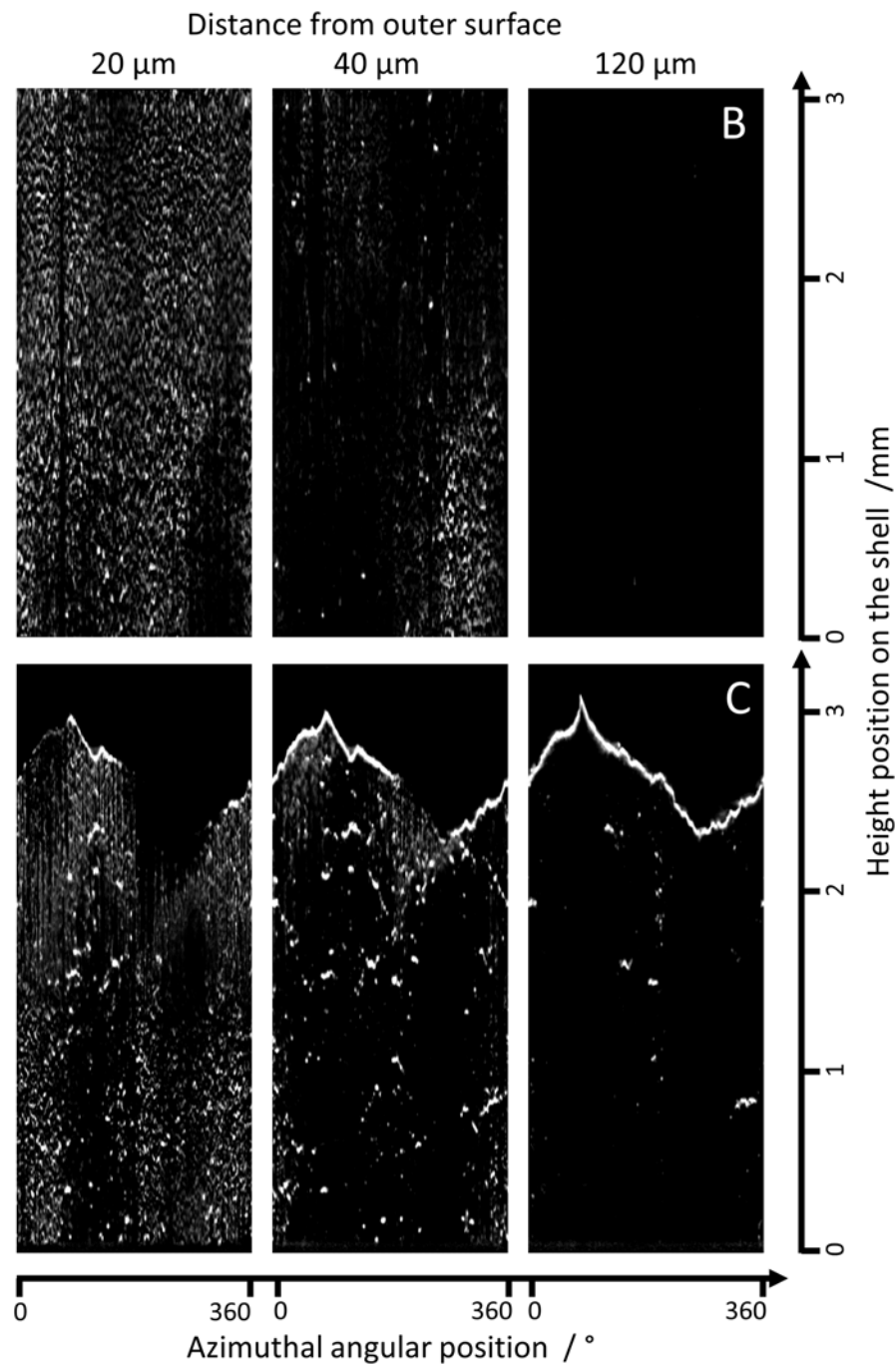


Figure 9. Unrolled concentric elliptical shells of the C_m reconstructions (see Figure 6 and 7) of specimens B (top) and C (bottom) at different distances from the outer surface. Intersections with the fracture surface of specimen C appear as prominent jagged lines. Note that in both specimens the frequency of cracks decreases toward the center and that cracks in specimen C extend to larger depth.

These findings are confirmed by metallographic images (optical microscopy), though with smaller statistics for the same FoV (see Figure 10).

Interestingly, Figure 10 shows that because of the hydrogen charging procedure, the outer surface of the specimens was very rough. The surface roughness (probably due to the electrochemical charging) is not necessarily the main reason for crack

initiation. In fact, the hydrogen concentration is usually highest at the surface and decreases toward the interior. Most probably, the rougher surface and the higher hydrogen concentration both play a role on failure. A detailed study of the roughness is, however, beyond the scope of the present work, as it would require many more data.^[30] The results in Figure 7 and 8 show that the major portion of the damage is initially caused by the hydrogen

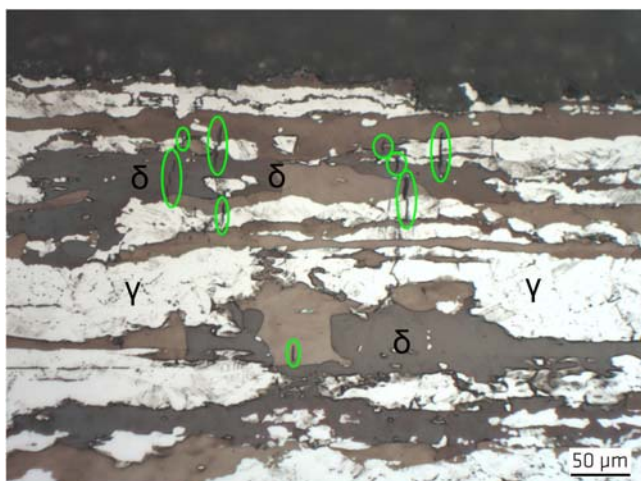


Figure 10. Metallographic images of hydrogen-charged and plastically deformed specimen B with Beraha II etching. Some cracks are highlighted.

charging procedure and little additional damage is introduced during plastic deformation (specimen B). However, a significant amount of damage (observed by SXRCT) arises at large elongations, i.e., shortly before failure (specimen C). A similar phenomenon was observed in Nellesen et al.^[26] and Kupsch et al.,^[31] where only the latest stages of deformation induced a measurable increase of damage.

4. Conclusions

We have demonstrated the complementarity of synchrotron X-ray refraction techniques (and in particular computed tomography, SXRCT) with respect to conventional absorption-based X-ray computed tomography (XCT or SXCT) in detecting and imaging defects. We tackled the particularly difficult problem of quantifying microcracking induced by a hydrogen charge in a duplex steel, as well as the damage evolution after application of external stress. We found that microcracks propagate only in the latest stages of plastic deformation (just before rupture), and that damage induced by hydrogen concentrates at the surface of charged specimens. Finally, we demonstrated that superior information content was obtained by X-ray refraction techniques in terms of image contrast and detectability. Through the use of the X-ray refraction 3D CT reconstructions, we could extract crack size distributions and distances to the external surface based on a large number of defects, i.e., statistically relevant ensembles, otherwise not detectable with absorption-based XCT. While in situ studies (under applied load) would be necessary to give more details and possibly cast light on the damage evolution of hydrogen-charged materials, our work paves the road to the detailed understanding of damage mechanisms in hydrogen-charged and many other materials under service conditions (temperature, load).

Acknowledgements

This work was financially supported by “Bundesanstalt für Materialforschung und -prüfung (BAM)” within the internal program

Ideen_2013_25. The authors thank Daniel Stock for technical support, Michaela Buchheim for SEM investigations, and Mareike Kirstein and Marina Marten for metallographic analysis (all BAM colleagues).

Open access funding enabled and organized by Projekt DEAL.

Conflict of Interest

The authors declare no conflict of interest.

Data Availability Statement

The data that support the findings of this study are available from the corresponding author upon reasonable request.

Keywords

2101 duplex stainless steel, computed tomography, fractography, hydrogen embrittlement, microcracking, synchrotron radiation, X-ray refraction

Received: September 22, 2021

Revised: January 7, 2022

Published online:

- [1] a) A.-A. Iris, *Recent Patents Mech. Eng.* **2008**, 1, 51; b) M. Liljas, presented at 6th, *European Stainless Steel Conf.; Science and Market; Proc.*, Stockholm, Helsinki, Finland, **2008**; c) M. F. McGuire, *Stainless Steels for Design Engineers*, ASM International, Materials Park, OH **2008**.
- [2] M. Knyazeva, M. Pohl, *Metallogr. Microstruct. Anal.* **2013**, 2, 113.
- [3] F. Zucchi, V. Grassi, C. Monticelli, G. Trabaneli, *Corros. Sci.* **2006**, 48, 522.
- [4] S.-L. Chou, W.-T. Tsai, *Mater. Chem. Phys.* **1999**, 60, 137.
- [5] a) R. A. Oriani, *Berichte Bunsengesellschaft Phys. Chem.* **1972**, 76, 848; b) A. R. Troiano, *Trans. ASM* **1960**, 52, 54.
- [6] a) J. He, L. Chen, X. Tao, S. Antonov, Y. Zhong, Y. Su, *Corros. Sci.* **2020**, 176, 109046; b) J. C. Villalobos, A. Del-Pozo, J. Mayen, S. Serna, B. Campillo, *Int. J. Hydrogen Energy* **2020**, 45, 9137.
- [7] a) T. Michler, J. Naumann, *Int. J. Hydrogen Energy* **2010**, 35, 1485; b) Y. Mine, T. Kimoto, *Corros. Sci.* **2011**, 53, 2619.
- [8] a) L. Claeys, T. Depover, I. D. Graeve, K. Verbeken, *Mater. Character.* **2019**, 156, 109843; b) L. Claeys, I. D. Graeve, T. Depover, K. Verbeken, *Mater. Sci. Eng. A* **2020**, 797, 140079.
- [9] J. O. Nilsson, G. Chai, presented at *World Conf.; 5th, Duplex Stainless Steels*, Zutphen, Maastricht; The Netherlands, **1997**.
- [10] M.-C. Marinelli, A. El Bartali, J. W. Signorelli, P. Evrard, V. Aubin, I. Alvarez-Armas, S. Degallaix-Moreuil, *Mater. Sci. Eng.: A* **2009**, 509, 81.
- [11] C. San Marchi, B. P. Somerday, J. Zelinski, X. Tang, G. H. Schiroky, *Metall. Mater. Trans. A* **2007**, 38, 2763.
- [12] R. Oltra, C. Bouillot, T. Magnin, *Scr. Mater.* **1996**, 35, 1101.
- [13] O. Sobol, G. Holzlechner, G. Nolze, T. Wirth, D. Eliezer, T. Boellinghaus, W. E. S. Unger, *Mater. Sci. Eng.: A* **2016**, 676, 271.
- [14] B. Gołębowski, W. A. Świątnicki, M. Gaspérini, *J. Microsc.* **2010**, 237, 352.
- [15] X. Z. Liang, G. H. Zhao, M. F. Dodge, T. L. Lee, H. B. Dong, P. E. J. Rivera-Díaz-del-Castillo, *Materialia* **2020**, 9, 100524.
- [16] M. Castellote, J. Fulla, P. G. de Viedma, C. Andrade, C. Alonso, I. Llorente, X. Turrillas, J. Campo, J. S. Schweitzer, T. Spillane, R. A. Livingston, C. Rolfs, H.-W. Becker, *Nucl. Inst. Methods Phys. Res., B* **2007**, 259, 975.

- [17] N. J. H. Holroyd, T. L. Burnett, M. Seifi, J. J. Lewandowski, *Mater. Sci. Eng. A* **2017**, *682*, 613.
- [18] K. Eguchi, T. L. Burnett, D. L. Engelberg, *Corros. Sci.* **2021**, *184*, 109363.
- [19] B. R. Müller, R. C. Cooper, A. Lange, A. Kupsch, M. Wheeler, M. P. Hentschel, A. Staude, A. Pandey, A. Shyam, G. Bruno, *Acta Mater.* **2018**, *144*, 627.
- [20] a) B. R. Müller, A. Lange, M. Harwardt, M. P. Hentschel, *Adv. Eng. Mater.* **2009**, *11*, 435; b) A. Kupsch, B. R. Müller, A. Lange, G. Bruno, *J. Eur. Ceram. Soc.* **2017**, *37*, 1879.
- [21] R. Laquai, T. Schaupp, B. R. Müller, A. Griesche, A. Kupsch, A. Lange, T. Kannengiesser, G. Bruno, *presented at Proc. of the 19th World Conf. on Non-Destructive Testing 2016*, Munich, Germany **2016**.
- [22] A. M. Elhoud, N. C. Renton, W. F. Deans, *Int. J. Hydrogen Energy* **2010**, *35*, 6455.
- [23] a) M. Rhode, *Dissertation, BAM-Dissertationsreihe*, Band 148, **2016**; b) S. Salmi, M. Rhode, S. Jüttner, M. Zinke, *Weld. World* **2015**, *59*, 137; c) T. Schaupp, W. Ernst, H. Spindler, T. Kannengiesser, *Int. J. Hydrogen Energy* **2020**, *45*, 20080.
- [24] W. Görner, M. P. Hentschel, B. R. Müller, H. Riesemeier, M. Krumrey, G. Ulm, W. Diete, U. Klein, R. Frahm, *Nucl. Instr. Methods Phys. Res. Sect. A: Acceler. Spectrometers Detectors Assoc. Equipment* **2001**, 467–468, 703.
- [25] R. Laquai, B. R. Müller, J. A. Schneider, A. Kupsch, G. Bruno, *Metall. Mater. Trans. A* **2020**, *51*, 4146.
- [26] J. Nellesen, R. Laquai, B. R. Müller, A. Kupsch, M. P. Hentschel, N. B. Anar, E. Soppa, W. Tillmann, G. Bruno, *J. Mater. Sci.* **2018**, *53*, 6021.
- [27] a) S. Cabeza, B. R. Müller, R. Pereyra, R. Fernandez, G. Gonzalez-Doncel, G. Bruno, *J. Appl. Crystallogr.* **2018**, *51*, 420; b) R. Laquai, B. R. Müller, G. Kasperovich, J. Haubrich, G. Requena, G. Bruno, *Mater. Res. Lett.* **2018**, *6*, 130.
- [28] a) A. Lange, M. P. Hentschel, A. Kupsch, B. R. Müller, *Int. J. Mater. Res.* **2012**, *103*, 174; b) A. A. M. Al-Falahat, A. Kupsch, M. P. Hentschel, A. Lange, N. Kardjilov, H. Markötter, I. Manke, *Rev. Sci. Instr.* **2019**, *90*, 125108.
- [29] A. P. Soares, D. Baum, B. Hesse, A. Kupsch, B. R. Müller, P. Zaslansky, *Dent Mater.* **2021**, *37*, 201.
- [30] T. Fritsch, L. Farahbod-Sternahl, I. Serrano-Muñoz, F. Léonard, C. Haberland, G. Bruno, *Adv. Eng. Mater.* **2021**, 2100689.
- [31] A. Kupsch, V. Trappe, B. R. Müller, G. Bruno, *IOP Conf. Ser.: Mater. Sci. Eng.* **2020**, *942*, 012035.